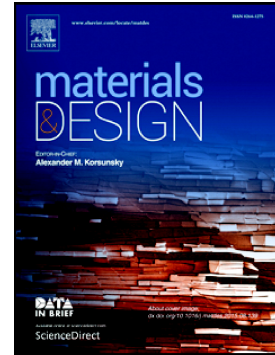


Journal Pre-proof

Investigation of the in situ thermal conductivity and absorption behavior of nanocomposite powder materials in laser powder bed fusion processes



O. Pannitz, A. Lüddecke, A. Kwade, J.T. Sehr

PII: S0264-1275(21)00083-6

DOI: <https://doi.org/10.1016/j.matdes.2021.109530>

Reference: JMADE 109530

To appear in: *Materials & Design*

Received date: 14 July 2020

Revised date: 13 January 2021

Accepted date: 24 January 2021

Please cite this article as: O. Pannitz, A. Lüddecke, A. Kwade, et al., Investigation of the in situ thermal conductivity and absorption behavior of nanocomposite powder materials in laser powder bed fusion processes, *Materials & Design* (2021), <https://doi.org/10.1016/j.matdes.2021.109530>

This is a PDF file of an article that has undergone enhancements after acceptance, such as the addition of a cover page and metadata, and formatting for readability, but it is not yet the definitive version of record. This version will undergo additional copyediting, typesetting and review before it is published in its final form, but we are providing this version to give early visibility of the article. Please note that, during the production process, errors may be discovered which could affect the content, and all legal disclaimers that apply to the journal pertain.

© 2021 Published by Elsevier.

Investigation of the in situ Thermal Conductivity and Absorption Behavior of Nanocomposite Powder Materials in Laser Powder Bed Fusion Processes

O. Pannitz^{a,*}, Oliver.Pannitz@ruhr-uni-bochum.de, A. Lüddecke^b, A. Kwade^b, J. T. Sehr^a

^aRuhr University Bochum, Chair of Hybrid Additive Manufacturing, Universitätsstr. 150, 44780 Bochum, Germany

^bTechnical University Braunschweig, Institute for Particle Technology, Volkmaroder Str. 5, 38104 Braunschweig, Germany

*Corresponding author.

Abstract

One of the AM processes for direct manufacturing of metallic components is powder bed fusion of metals using a laser beam system (PBF-LB/M), in which metallic powders are molten and solidified in a layer upon layer manner by a focused laser beam. In recent years, the focus has initially been on increasing the efficiency of the systems itself. However, the modification of standard AM metal alloys using nanoparticles offers the possibility to improve the PBF-LB/M-process concerning its process efficiency and actual densification and thermal conductivity. In this work, a methodology for an in-situ investigation of the thermal conductivity as well as the reflectance behavior of metallic powder materials during the PBF-LB/M-process is established. The powder material stainless steel 1.4404 was coated with different nanoparticles (few-layer graphene (FLG), silicon carbide (SiC)) and processed in a standardized build process. As a result, the reflectance rate of all modified materials could be increased. Besides, the thermal conductivity of the material is attested to be a decisive and influencing factor for the quality of the final component. Thus, an improved relative density was achieved using the FLG/1.4404 and SiC/1.4404 (1 vol.%) due to the increased thermal conductivity of the material. Also significant defects in the cross section were visible at SiC/1.4404 (4 vol.%).

Keywords: Additive manufacturing, PBF-LB/M, Stainless steel (1.4404, 316L), Nanocomposite, Absorption, Infrared thermography

1. Introduction

An additive manufacturing (AM) process is described as the incremental layer upon layer build-up of a three-dimensional workpiece and represents the third category next to subtractive and formative manufacturing [1]. This, in turn, leads to significant benefits, such as increased freedom of design, the realization of complex structures, and the integration of functions. One of the AM processes for direct manufacturing of metal parts is powder bed fusion of metals using a laser beam system (PBF-LB/M), in which metallic powders are molten and solidified in a layer upon layer manner by a focused laser beam [2]. The industry shows great interest in AM of metallic components, which is illustrated by rising sales figures for systems [3]. 1.4404 (EN: 14404 / X2CrNiMo17-12-2 / AISI 316L) is a stainless, austenitic steel and one of the most commonly used steels in a PBF-LB/M-system. The material is applied to a wide range of industrial areas, such as oil and gas, automotive, aerospace, and biomedical engineering, due to its high strength, ductility, corrosion resistance, and biocompatibility [4,5]. Recently, more and more PBF-LB/M-systems are equipped with bigger build chambers, multiple lasers, or high power laser systems in order to increase process efficiency. Along with these developments, machine prices increase significantly. Thus, apart from processing standard AM powder materials, great research efforts addressed the integration of nanoparticles and the manufacturing of nanocomposite parts. The modification of metal alloys using nanoparticles offers the possibility to improve the PBF-LB/M-process concerning its efficiency and the subsequent component quality including mechanical properties and microstructural characteristics.

Gu et al. [6] processed Ti metal powder for PBF-LB/M-processes with nanoparticle reinforcements. One focus of the study was the investigation of TiC/Ti parts. The TiC/Ti nanocomposite was prepared

in a vario planetary mill containing 15 wt.% TiC. After the determination of a sufficient process window to reach relative part densities above 97 %, the reinforced parts exhibit an increased dynamic microhardness, elastic modulus and decreased wear rate. Comparable results were obtained with a TiC content of 12.5 wt.% [7]. Gu et al. [8] also compared ball-milled TiC/Ti nanocomposite powder and mechanically mixed nano-TiC/Ti powder and investigated the influence of nanopowder characteristics and processing parameters on densification, microstructural and mechanical properties. As a result, the densification of the ball-milled nanocomposites was higher than the mechanically mixed nano-TiC/Ti powder. Further investigations concerning TiC-reinforced AlSi10Mg were conducted by Gu et al. [9,10]. TiC was also used to reinforce stainless steel 1.4404 in multiple research activities from Al Mangour et al. [11,12]. Four different TiC/1.4404 nanocomposites containing a volume fraction from 2.5 to 15 vol.% were prepared with two different starting TiC particle sizes (1 μm and 50 nm) by ball milling. A vario-planetary mill was used as a mixing process. At first, the influence of different particle sizes and volume contents of TiC on constitutional phases, microstructural and mechanical properties was investigated. Consequently, an increased relative density was obtained with use of fine particles at a low volume content due to an improved wettability. Furthermore, the hardness values increased and the coefficient of friction as well as wear rate decreased at an increased TiC volume content due to the combined effect of grain refinement and grain boundary strengthening [11]. In a further investigation, Al Mangour et al. [12] present a correlation between volume energy density and TiC particle size and validates a simulation to predict the temperature evolution and thermal behavior of the melt pool. Subsequently, TiC particle size increases simultaneously to an increasing volume energy density due to thermal accumulation within the melt pool. TiB₂/1.4404 was also processed with varying nanoparticle content by Al Mangour et al. [13]. An increased hardness, yield strength and decreased coefficient of friction and wear rates with a strong dependency on TiB₂ volume content could be observed. Further reinforced 1.4404 manufactured by PBF-LB/M were investigated by Zhao et al. [14], Wilms et al. [15] and Salman et al. [16]. Chang et al. [17] studied the influence of different particle sizes in a SiC/AlSi10Mg composite powder on the microstructure and mechanical properties of PBF-LB/M-parts. Therefore, superior material characteristics concerning densification and microhardness were achieved by using the smallest SiC particle size. In addition, Sehrt et al. [18] processed Al₂O₃ nanoparticles on feedstock material tool steel (1.2709) and Hastelloy X (2.4665) and investigated its melt pool dynamics and microstructural properties. Both nanocomposites show a significant improvement of mechanical properties and nanoparticles form agglomerates that determine the melt pool dynamics. A similar approach was performed by Sehrt et al. [19] by modifying tool steel with WC and TiO₂ nanoparticles.

It is evident that material-based input parameters, such as sphericity, particle size distribution, flowability, and reflectance, are essential to ensure a defect-free process and reproducible component quality [20,21]. Especially the laser-material-interaction is of great interest. Zhou et al. [22] proved that Al₂O₃-coated metallic powders exhibit higher laser absorptivity with respect to uncoated metallic powders due to an increased surface roughness of the particles. Yang et al. [23] investigated the absorption behavior of AlSi12 powder and its correlation to different particle sizes. As a result, the dependence of both parameters was visible. With an increasing particle size, the absorption of the laser beam decreases. A similar result was reported by Gu et al. [24], who compared the absorption behavior of SiC and TiB₂-reinforced AlSi10Mg. The reinforced material exhibited an increased absorption behavior compared to the original feedstock material, due to multiple scattering of the laser beam. Furthermore, a simulation created by Boley et al. [25] demonstrates and proves the mentioned correlation between absorption, particle size distribution and geometry. Tolochko et al. [26] also investigated the laser absorption of different powder materials including metals and ceramics. A change in absorption is observed with increasing exposure time by the laser beam. Using an Ni-alloy, the powder is heated by an Nd:YAG laser causing the material to be partially sintered at first. The surface of the powder particles melts and results in a rearrangement within the powder bed. During the subsequent melting of the metal powder, the porosity of the powder bed is suddenly reduced, resulting in a significant decrease in absorption capacity.

Additionally, process monitoring systems (e.g. thermographic camera, high-speed camera, etc.) can be used to detect defects and irregularities during the process. In past scientific work, the implementation of infrared cameras on PBF-LB/M-systems has already been accomplished. This primarily serves the purpose of non-contact, non-destructive testing of components by detecting build-up defects, such as pores or binding defects during the AM process [27,28]. Microstructural defects can have a significant influence on mechanical properties of the manufactured components. Krauss et al. [28] discovered that defects in the microstructure can be detected if they occur for a period of more than 20 ms and are compared with predefined reference limits. Cracks with a length of 40 – 500 μm can be detected by applying an infrared camera. Furthermore, the in-situ material behavior can be characterized. A complex challenge when implementing an infrared camera is the required calibration of the camera system. Influencing factors which lead to a change in emissivity and thus, complicate the calibration of the system are, for example, the varying roughness and oxidation of the powder surface, the viewing angle, the temperature and the utilized material [29]. Körperich et al. [29] conducted a thermal analysis of the build-up height on mechanical properties of hot-working steel during the PBF-LB/M-process. Using an infrared camera, they were able to detect a drop in temperature of up to 170 $^{\circ}\text{C}$ over the entire build height. At the same time, the effect on the hardness could be determined, which could also be observed in dependence of the build height. The development of the hardness values varied between 614 HV_{10} and 662 HV_{10} .

In the research environment, studies have been performed on the conductivity of different metal powders. They established that the thermal conductivity of metallic powder materials is strongly dependent on the powder size, the morphology and the cavity between powder particles [30]. The thermal conductivity describes how rapidly the thermal energy is conducted through the metallic solidified material and, before consolidation, is an indicator for the heat from irradiated powder conducted to other adjacent powder particles. Depending on the material, the energy input can be adjusted in respect of thermal energy in order to achieve a homogeneous melting process. [31,32] In this context, Buchbinder et al. [33] state that materials with high thermal conductivity can be processed with an increased energy density. Typically, cooling rates of approx. 10^5 to 10^7 K/s are achieved during the PBF-LB/M-process [31]. Furthermore, research has already been conducted on the correlation between process parameters and thermal conductivity. For instance, Simmons et al. [34] have investigated the correlation between the porosity of bulk metallic components manufactured by PBF-LB/M and thermal conductivity. In this case, the thermal conductivity was measured by frequency domain thermoreflectance (FDTR) and the specimens were made of stainless steel 1.4404. As a conclusion, an increased thermal conductivity leads to increased densification of the bulk material. At the same time, the thermal properties are influenced by varying process parameters. These findings are in accordance with the results of Alkahari et al. [32]. Here, a methodology for the determination of thermal conductivity has been developed, in which a voltage is measured using a thermocouple as the energy input in a bulk powder increases. Furthermore, it was found that the bulk density and the particle diameter of metal powder represents a significant influencing parameter concerning the thermal conductivity.

In this work, a methodology for an in-situ investigation of the thermal conductivity as well as the reflectance behavior of the metallic powder materials during the PBF-LB/M-process is established. For this purpose, an infrared camera is implemented in the build chamber of the PBF-LB/M-system. Based on this, standardized build processes are performed with varying metal powders. The materials are, on the one hand, the austenitic, stainless steel 1.4404 and, on the other hand, modified types of this powder. The modification affected the coating with two different nanoparticle materials (few-layer graphene (FLG) and silicon carbide (SiC)) in order to achieve an improvement of thermal conductivity, reflectance behavior and densification behavior.

2. Materials and Methods

2.1. Powder Material

2.1.1. Feedstock material

Gas atomized stainless steel 1.4404 (X2CrNiMo17-12-2) powder was used as a feedstock, which was then coated with silicon carbide (SiC) and few-layer graphene (FLG) to achieve a modification of the thermal conductivity and reflectance behavior. According to DIN EN 10088-1 [35], the chemical composition of 1.4404 is presented in Table 1.

Table 1: Nominal chemical composition of 1.4404 stainless steel powder [35]

Element	Fe	Cr	Ni	Si	Mo	Mn	P	S	C
Content in wt. %	bal.	16.5 – 18.5	10.0 – 13.0	max. 1.0	2.0 – 2.5	max. 2.0	max. 0.0045	max. 0.015	max. 0.03

The Mastersizer 3000 dry module (Malvern) was used for the PSD analysis of the dry AM powder and dry coated powders. Therefore, a dispersing pressure of 2 bar and optical concentration between 2 and 5 % was chosen (cf. Figure 1c).

Particle size distributions smaller than 600 nm were measured with the Nanophox (Sympatec GmbH) via dynamic light scattering (according to DIN ISO 22412 [36]), therefore the samples were diluted in the same solvent as used in the grinding experiments. The measurements were conducted at 25 °C at a count rate between 500 and 1000. The powder morphology was analyzed by the scanning electron microscope (SEM) Gemini2 Merlin by Carl Zeiss AG (Germany). The different powders were steamed with 15 nm of gold to increase electrical conductivity. Additional measurements were performed with the SEM Helios G4 CX (FEI/ThermoFisher Scientific).

2.1.2. Additive formulation and coating process

The SiC and few-layer graphene (FLG) were processed in an aqueous medium via stirred media milling (Labstar, Netzsch (Germany)). For SiC grinding high circumferential speeds of 12 m/s and small grinding beads (200 μm) with a density of 3910 kg/m^3 were applied. Additionally, an electrostatic stabilization with HNO_3 (pH: 4.4) was utilized in order to prevent the nanoparticles from agglomeration. In the case of FLG, low circumferential speeds of 4 m/s and grinding beads (400 μm) with a density of 4100 kg/m^3 were used in order to delaminate the graphite flakes and not to induce lateral fractures. To prevent the FLG from agglomeration, a steric stabilization was used (Kollidon 30, BASF). The resulting suspension was centrifuged in 50 ml falcon tubes for 8 min and 4000 rpm to ensure that no unprocessed graphite is present in the suspension. Both suspensions were stored in a shaking plate and remained stable without any visible agglomeration or sedimentation. For validation purposes the zeta potential was measured with electroacoustic measurements (DT, Dispersion Technology Inc., USA) in the original suspension at room temperature. A fluidized bed (Mini-Glatt, Glatt GmbH (Germany)) with top spray configuration was used for the coating experiments. The process was designed in order to maintain a stable fluidized bed during the coating experiments (s. Table 2). Coating coverages of 1.0 vol.% and 4.0 vol.% were produced for SiC and 0.75 vol.% for FLG. The required coating amounts of SiC particles were chosen on a theoretically based assumption. A volume fraction of 1 vol.% corresponds to a mass concentration of 0.4 wt.% and a theoretical surface coverage of 100 %. For the calculation of the theoretical surface coverage, the host and guest particle size was assumed spherical and a densest ball packing was calculated according to the assumptions made in [37].

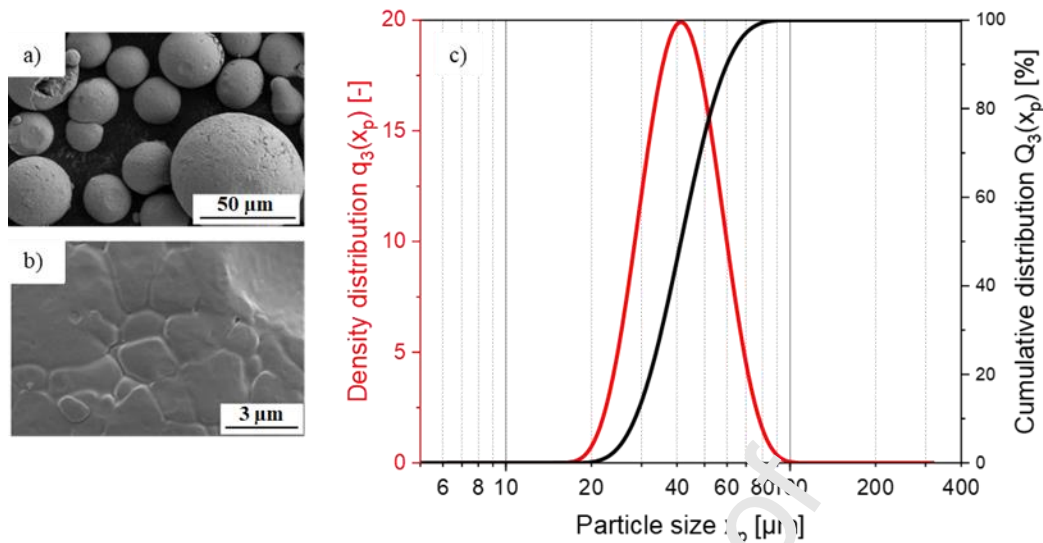


Figure 1: Uncoated feedstock material 1.4404 a), b) SEM images and c) particle size distribution

Table 2: Fluidized bed coating process parameters

	SiC	FLG
Pressure drop of airflow [bar]	0.6	0.6
Pressure drop of nozzle [bar]	0.7	0.9
Temperature [°C]	80	
Filter cartridges cleaning intervall [s]	2	
Spray rate [ml/min]	1	

2.1.3. Reflectance measurement

The reflectance measurement of the samples was analyzed by the Nicolet iS20 FTIR spectrometer from Thermo Fisher Scientific (USA). The DiffusIR from Pike was used as an accessory for the measurement. The measurements were carried out at room temperature. An aluminum mirror served as a reference for the background measurement. All spectra were recorded using a white light source, an XT-KBr beam splitter, and an MTEC detector range of 4000 to 11000 cm^{-1} with 64 scans and a spectral resolution of 4 cm^{-1} . During sample preparation, a cup (diameter: 5 mm; depth: 3 mm) is filled with the powder material to be measured. The subsequent removal of the excess powder with the support of a blade leads to a similar application behavior to that of the PBF-LB/M-process, so that a reproducible reflectance measurement is guaranteed. Three spectra from each of the four samples were recorded to check the reproducibility of the measurement. The wavenumber of 9398 cm^{-1} (reciprocal value of the wavelength) corresponds to a wavelength of $\lambda = 1064 \text{ nm}$ which equals the wavelength of Nd:YAG laser utilized in a PBF-LB/M system.

2.2. Processing

2.2.1. PBF-LB/M-system

The metallic samples were manufactured using the PBF-LB/M-system TruPrint 1000 of Trumpf GmbH & Co. KG (Germany). The TruPrint 1000 is equipped with an Nd:YAG fiber laser (wavelength of $\lambda = 1064 \text{ nm}$) with a maximum laser power of 200 W and focal diameter of 30 μm . An F-theta lens ensures that the focal point of the laser beam is positioned in the working plane. The system enables a maximum build size of 100 mm (diameter) and a height of 100 mm. Furthermore, the components and the powder inside of the build chamber are protected against oxidation by a nitrogen atmosphere. The recoating mechanism consists of a rubber x-profile and distributes a thin layer of metal powder from the feed region over the build platform. Afterwards, the applied layer is selectively molten according to the cross-sections of the parts and metallurgically bonded to the underlying layer. As soon as this

step is completed, the build platform is lowered and a new layer of powder is applied. These steps are repeated until the parts are finished.

2.2.2. Standardized build process

A standardized build process with three test specimens (cf. Figure 2) was designed and manufactured. In order to investigate the influence of the component height on the temperature development, the first specimen represents a cylinder with a diameter of 8 mm and a height of 16 mm. In order to be able to observe up- and downskin effects, two cones were designed, which differ in the build-up process by a 180° rotation. The cones also measure 16 mm in height and have a conically reduced diameter from 8 mm to 2 mm. By choosing these dimensions, the cones can be manufactured without support structures, as the critical angle of 45° is not reached. In order to achieve comparability of the processed materials, these were manufactured with the same process parameters (cf. Table 3).

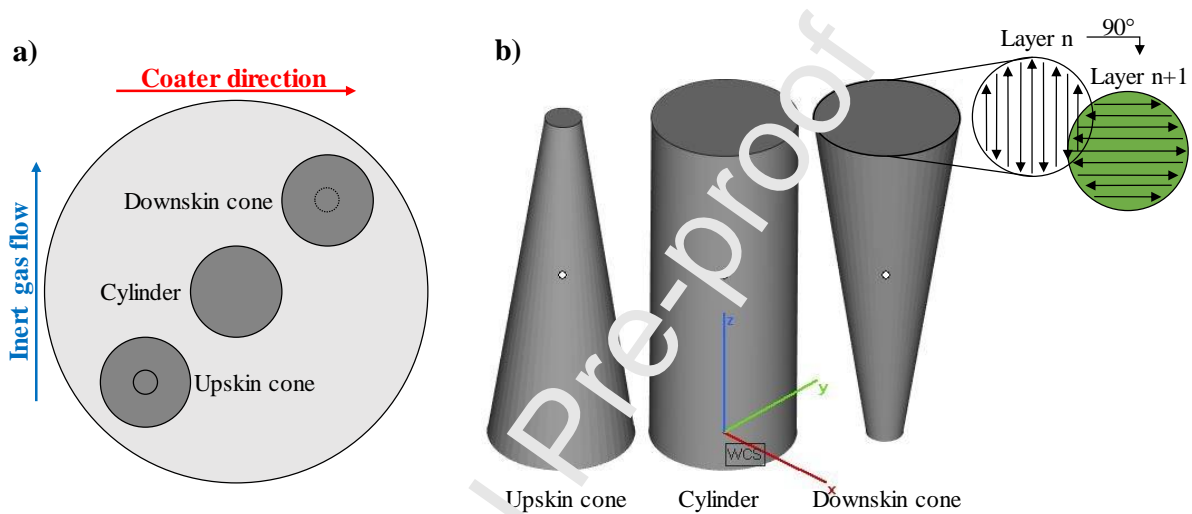


Figure 2: a) Specimen arrangement on the build plate (top view) b) 3D model of the standardized build job with an illustration of the applied scan strategy

Table 3. PBF-LB/M nominal process parameters and environment applied on 1.4404, SiC/1.4404 and FLG/1.4404

Laser power P_L	130 W
Hatch distance h_d	80 μm
Layer thickness D_s	30 μm
Scan speed v_s	700 mm/s
Volume energy density E_v	77,38 J/mm ³
Scan strategy	90° alternating
Focal diameter	30 μm
Inert gas atmosphere	N ₂
Gas flow rate	3 m/s
Recoating speed	80 mm/s
Coater type	Rubber x-profile

2.2.3. Infrared camera

The infrared camera PI 640 from Optris GmbH (Germany) is utilized, which covers a temperature range from -20 to 900 °C and exhibits an accuracy of $\pm 2\%$. The specific temperature range of the camera must be selected before each measurement. The three temperature ranges -20 to 100 °C, 0 to 250 °C and 150 to 900 °C are available. The spectral range of the camera extends between 7.5 – 13 μm and the refresh rate up to 32 Hz. The camera has a resolution of 640 x 480 pixels. It measures the infrared radiation emitted by objects and calculates the surface temperature on this basis. The two-dimensional detector measures the surface area and displays it as a thermographic image using standardized color scales. The radiometric processing of the image data allows a subsequent detailed image analysis with the comfortable software PIX Connect. The calibration of the camera is performed

outside the PBF-LB/M system. A highly-resistant reference sample with a constant, defined emissivity is applied to a heating plate. Afterwards, the corresponding powder is deposited on the heating plate with a defined layer thickness and heated up to the maximum temperature of 500 °C. The emissivity is now adjusted in temperature increments, whereby saturation is reached after a short period of time (cf. Figure 3a). When determining the emissivity, the surface and the degree of oxidation is attested to be a significant influencing factor [38]. Since the surface of the deposited powder layer does not show any noticeable differences for the infrared camera used in this work and since no significant oxidation effects occur at room temperature, almost identical emissivity values are measured. As the temperature increases, the affinity for oxidation becomes visible and leads to a change in the emissivity. Corresponding to the emissivity values, the increased SiC content of SiC/1.4404 (4 vol.%) has a different influence on the oxidation behavior and thus also on the emissivity with increasing temperature. The camera was attached to the inside of the protective glass inside of the PBF-LB/M-process chamber using a mounting stand. A digital inclinometer from HOLEX (Germany) was used to set a consistent viewing angle of the of 57.1° relative to build plate to ensure the reproducibility of the measurements (cf. Figure 3b).

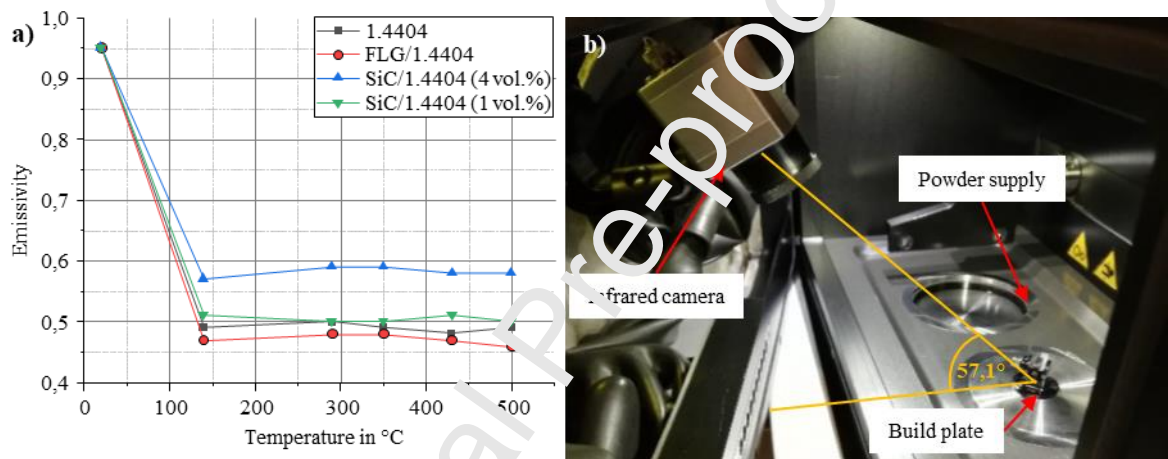


Figure 3: a) Emissivity of 1.4404 and its coatings under varying temperatures b) Positioning and mounting of the infrared camera inside of the TruPrint 1000 machine

In total, 533 layers were applied by the coater to manufacture the specimens. During the manufacturing process, the infrared camera is permanently pointed at the build plate, but the camera is only activated within certain layer ranges due to the immense volume of data. Since only one temperature spectrum can be selected for each measurement, the procedure shown in Table 4 was applied.

Table 4: Recorded temperature spectrums in dependence of the camera active layer ranges

Layer ranges	Recorded temperature spectrum	
	0 – 250 °C	150 – 900 °C
0 – 30	X	
60 – 90		X
125 – 150	X	
200 – 230		X
280 – 310	X	
360 – 390		X
400 – 430	X	
460 – 490		X
500 – 530	X	

2.3. Relative density

The Keyence VHX 6000 digital microscope of Keyence Corporation (Japan) was used to analyze the cross section and to quantify the relative density of the samples. The entire cross-section of the infill

section of a sample is recorded to evaluate and compare the relative density. The accumulated area of all pores can be recorded with the aid of particle/contamination analysis.

3. Results

3.1. Additive production and metal powder characteristics

The stirred media milling of SiC particles results in a median particle size of 99.3 nm (cf. Table 5). Zeta potential measurements of the suspension exhibit a value of 37.8 mV, indicating that the suspension is preserved against agglomeration. The produced FLG suspension exhibit a median particle size of 568.3 nm (cf. Table 5) and a zeta potential of -23.4 mV, which is a sufficient electrostatic barrier to prevent agglomeration [39].

As depicted in Figure 4 not the full surface is covered with SiC-particles, because of the loss of some material in the process and a slightly agglomeration of SiC particles. To investigate the influence of a complete covered surface on reflectance behavior of the laser light, flowability and heat conduction in the powder bed, the coating amount has been increased fourfold to ensure a complete coverage (cf. Figure 4). The relatively low coating amount of 0.75 vol.% of FLG was selected in order to ensure a thin layer of FLG flakes on the host particle surfaces and prevent agglomeration of the FLG's. In Figure 5 an occurred effect is depicted, where ring-like shapes are apparent. Most likely these shapes occur due to drying effects on the particle's surface at the presence of high volume fractions [40]. This effect is known as coffee-ring effect and are common whenever drops containing dispersed solids evaporate on a surface. The accumulation of particles on the edges of the droplet is thereby mainly caused by an outward flow of the liquid carrying solid particles due to faster evaporation of suspension in the peripheral area of the droplet [41–44].

A theoretical consideration of the carbon content in the alloy after PBF-LB/M results in 0.23 wt.% for 1.4404/FLG, for 1.4404/SiC (1 vol.%) 0.15 wt.%, for 1.4404/SiC (4 vol.%) 0.51 wt.%. The calculation is based on the content of FLG or SiC added on the metal particles weighted with the molecular carbon content plus 0.03 wt% of the feedstock carbon content. In further investigations the actual carbon content will be determined for instance by thermal analysis or ICP OES.

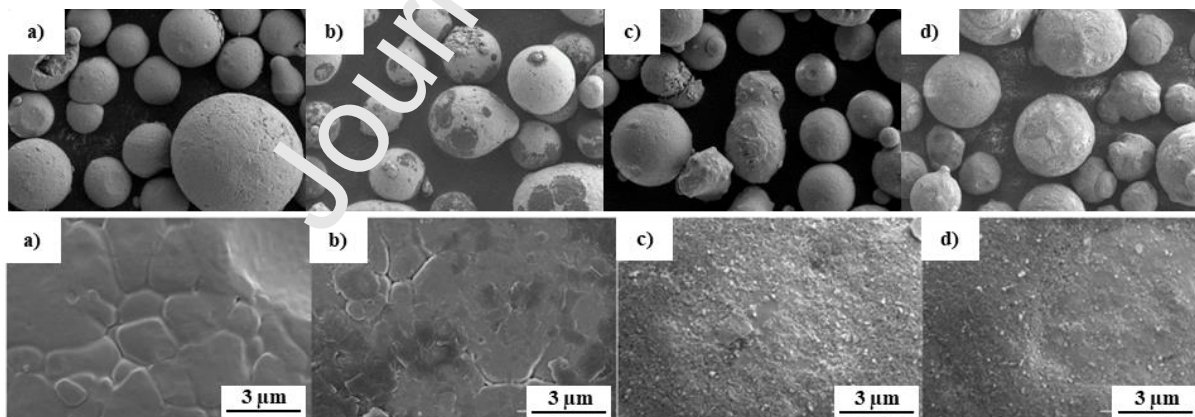


Figure 4: SEM-Images with different magnification of uncoated a) 1.4404 b) Graphene (0.75 vol.%, particle size 100 nm) and SiC surface coated coverages c) 1 vol.% d) 4 vol.%

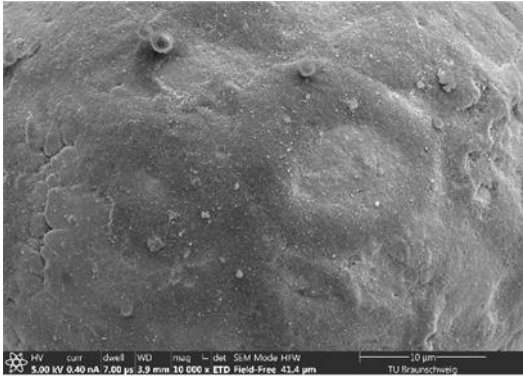


Figure 5: SEM-Image of coated 1.4404 (4 vol% SiC)

Table 5: Particle sizes of used suspensions, feedstock particles and coated particles

	SiC	FLG	1.4404	SiC/1.4404 (1 vol.%)	SiC/1.4404 (4 vol.%)	FLG/1.4404 (0,75 vol.%)
	Suspension [nm]		Dry particles [µm]			
Particle size						
X _{10,3}	65.2	363.8	28.3	29.2	29.9	27.3
X _{50,3}	99.3	568.3	41.3	42.3	43.7	40.4
X _{90,3}	160.8	890.3	60.1	61.2	63.1	60.2

3.2. Reflectance measurement

The results of the reflectance measurements are illustrated in Figure 6. Three measurements were taken for each material. It becomes clear that the alloy 1.4404 with an average value of approx. 11 % has the highest reflectance compared to the aluminum mirror. This is followed by the material SiC/1.4404 (1 vol.%) with approx. 9.4 % and the material FLG/1.4404 with 8.0 %. The material with the lowest reflectance of 6.4 % is represented by SiC/1.4404 (4 vol.%). It is shown that an increased amount of SiC leads to a decreased reflectance. The reflectance values are measured against an aluminum mirror as a reference material. However, since all four samples were measured against the same reference material, statements can still be made about the different reflectance behavior.

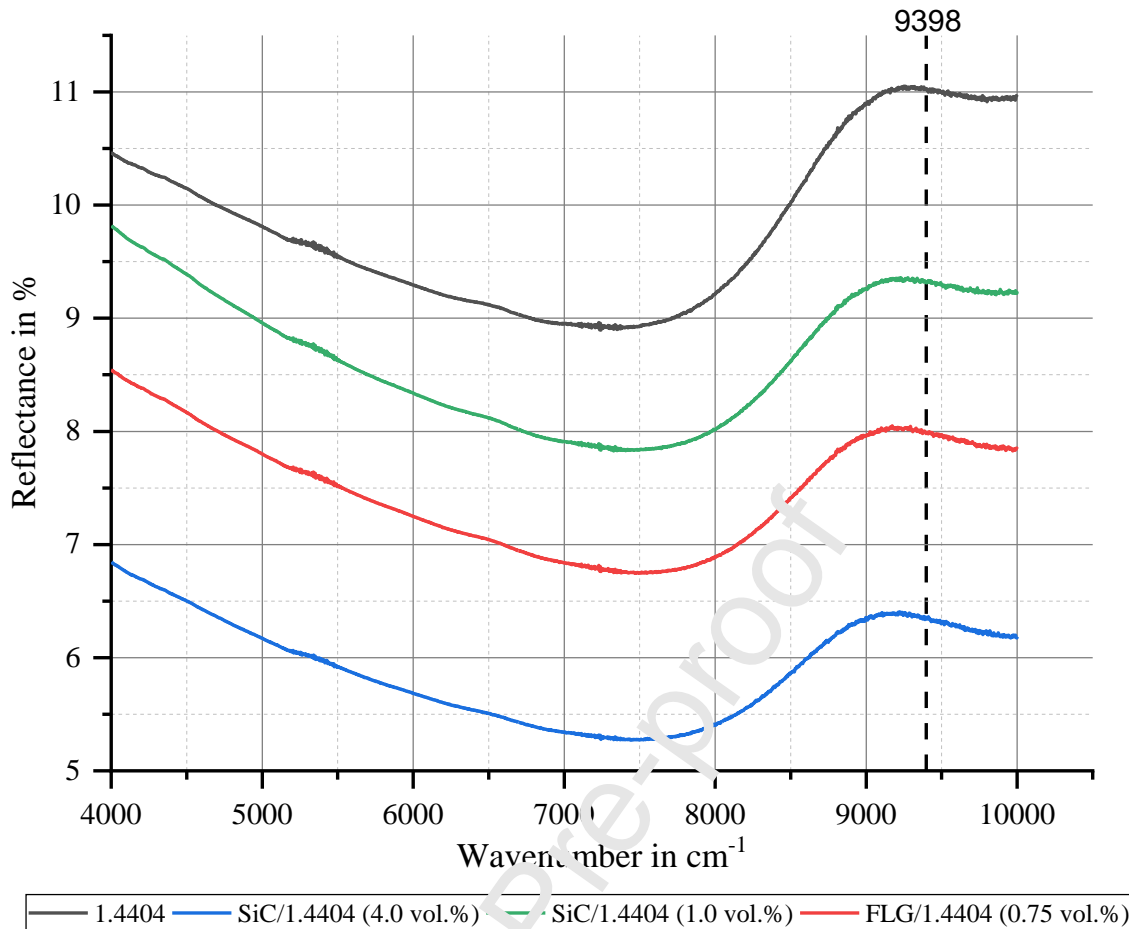


Figure 6: Reflectance measurements of stainless steel 1.4404 powder and its coatings; Reflectance was measured with respect to the wavenumber; wavenumber of 9398 cm^{-1} correspond to a wavelength of $\lambda = 1064 \text{ nm}$.

3.3. Temperature Distribution

The images illustrated in Table 6 were taken in the indicated layer ranges one frame after laser exposure ($1/32 \text{ s}$ at 32 Hz) and thus before the subsequent powder distribution. The direction of movement of the laser was from top right to bottom left as seen in the images. When comparing the images of the different powder materials in the initial layer ranges $0 - 10$ and $125 - 150$, it is noticeable that the SiC-coated metal powders cause a high heat distribution in the powder bed. Furthermore, it strikes that the surface area with temperatures above $250 \text{ }^\circ\text{C}$ is significantly more intense in both SiC/1.4404 (1 vol.%) and SiC/1.4404 (4 vol.%) powder materials. This difference is no longer clearly visible in the subsequent layers. In the images of FLG/1.4404, the high thermal conductivity of this material is visible. In Table 7 the quantification of the area percentage of a temperature level above $225 \text{ }^\circ\text{C}$ is illustrated. Here, an increase of the area percentage simultaneously to an increasing volume fraction of SiC and furthermore, decreased area percentage at the FLG-coating is clearly noticeable. Due to the established state of the process after 125 layers and increased information value, the layers $0 - 10$ were excluded in this table. Due to the high thermal conductivity, the generated heat seems to dissipate rapidly into the build plate, so that the heat distribution in the powder bed is significantly less compared to the other alloys. Since the heat in the powder bed does not disperse so far with the FLG-coating, there are significant differences in the thermal conductivity of powder materials and solids possible. In case of FLG/1.4404 a more stable process is guaranteed. In addition, the downskin geometry (located in the upper right corner) is the first exposed geometry by the laser. Assuming this, it should have the lowest temperatures due to the longest cooling time. In fact, however, the downskin cone of FLG/1.4404 exhibits increased temperatures in the layer range

400 – 430 compared to the cylinder and upskin cone. Another difference is the increased amount of spatters at SiC/1.4404 (4 vol.%) which can clearly be seen on the powder bed surface.

Table 6: Temperature distribution in the powder bed of stainless steel 1.4404 and its coatings

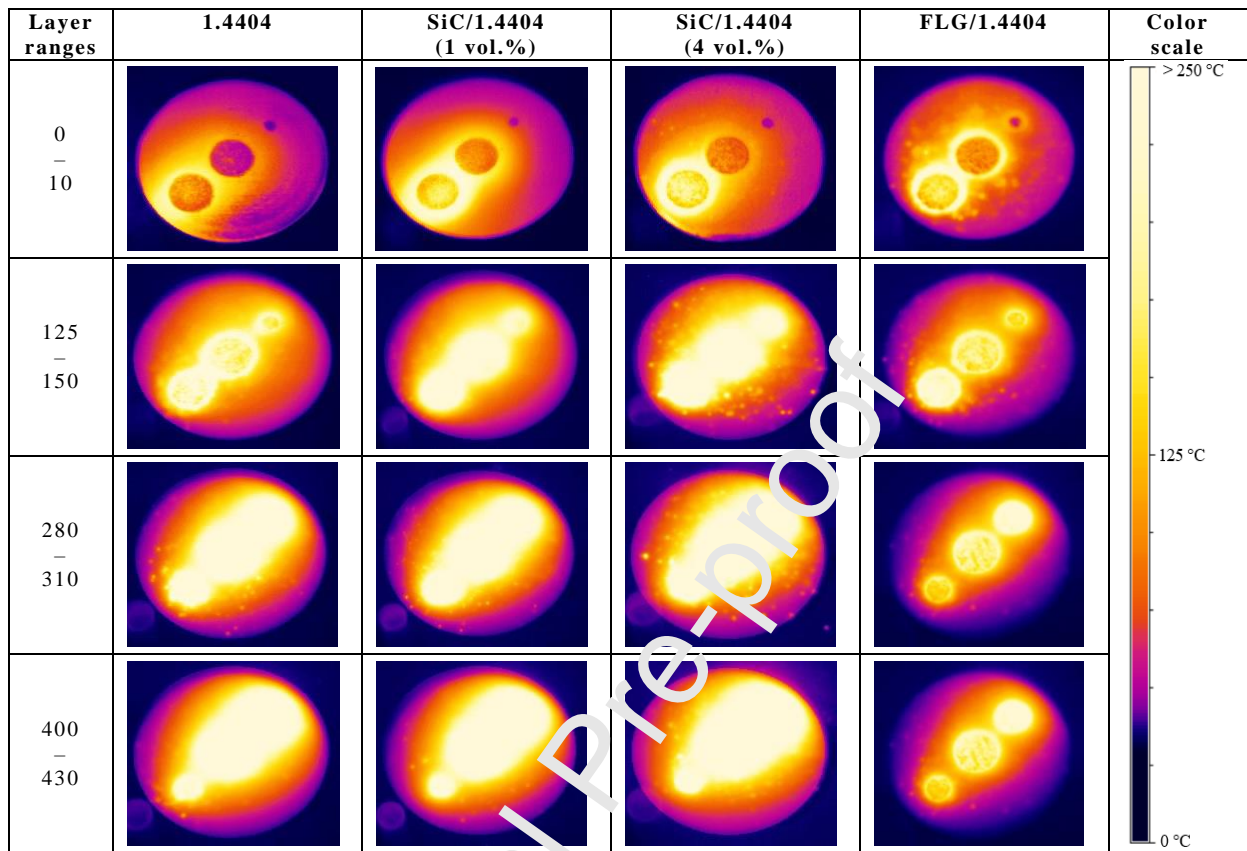
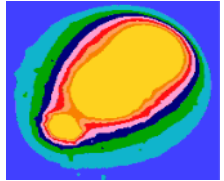
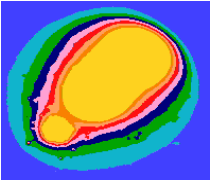
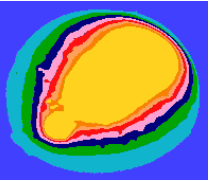
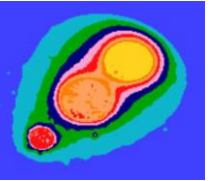
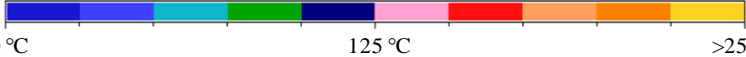


Table 7: Temperature distribution in the powder bed of stainless steel 1.4404 and its coatings with highlighted

	Material			
	1.4404	SiC/1.4404 (1 vol.%)	SiC/1.4404 (4 vol.%)	FLG/1.4404
Layer range 125 - 150				
Area percentage > 225 °C	9.43 %	13.08 %	13.65 %	0 %
Layer range 280 - 310				
Area percentage > 225 °C	12.72 %	17.94 %	18.96 %	0 %

surfaces above 225 °C for two different layer ranges

Layer range 400 – 430				
Area percentage > 225 °C	20.17 %	20.98 %	22.53 %	4.74 %
Color scale				

3.4. Temperature development in dependence on the component height

Within the layer ranges 60 – 90, 200 – 230, 360 – 390 and 460 – 490 a temperature spectrum of 150 – 900 °C was set in the infrared camera system. The obtained information allows statements to be made about the temperature development as a function of the component height for the individual materials. In order to be able to systematically observe the measured temperature values of the different alloys, geometries and powder layers, the ten highest temperature values per powder layer were determined for each alloy and geometry and the arithmetic mean value was calculated (cf. Figure 7).

It is noticeable that the measured temperatures for the alloy SiC/1.4404 (4 vol.%) are significantly higher than those for the other alloys. This is particularly evident in the layer ranges 60 – 90 and 200 – 230. In particular, the cylinder and the downskin cone are characterized by the maximum detectable temperature of 925 °C. The maximum temperature difference between the upskin cones of SiC/1.4404 (4 vol.%) and FLG/1.4404 exists in the layer range 460 – 490 (882.61 °C to 402.64 °C). In addition, the downskin cones of all four alloys show a temperature increase with increasing component height. Thus, the average maximum temperature of the downskin cone of the feedstock 1.4404 increases from 505.2 °C (layer 69 – 90) to 925 °C (layer 460 – 490). The temperature drop of the upskin cones of all alloys is equally noticeable with increasing heights. Thus, the average maximum temperature of the upskin cone of 1.4404 decreases from 696.77 °C (layer range 60 – 90) to 542.91 °C (layer range 460 – 490). Furthermore, the average maximum temperature of the cylinder varies at least over the height of the component. Considering the alloys 1.4404 and SiC/1.4404 (1 vol.%), there is only a temperature increase of 37.17 °C and 109.89 °C respectively over the entire height of the component. For the alloy FLG/1.4404 the corresponding value results in 21.26 °C.

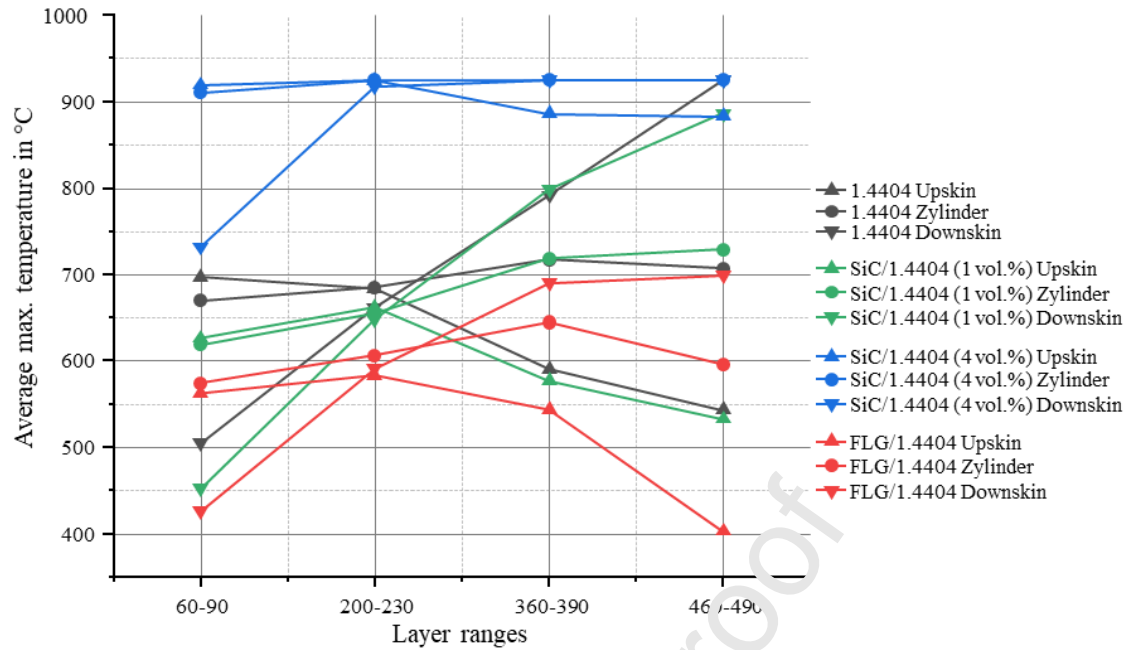


Figure 7: Average max. temperature development in dependence on component height

3.5. Optical Evaluation

A comparison of the geometries manufactured from the different powder material combinations reveals significant optical differences in the component surfaces (cf. Figure 8). The component of the original feedstock 1.4404 exhibits an apparently dense homogeneous surface without any detectable cracks and pores. Only a few weld spatters are visible. However, the annealing colors of the cylinder and the downskin cone can be seen. The annealing colors are visible on the cylinder from about half the height of the component and on the cone over the entire height. A highly homogeneous surface structure can be seen in components made of the alloy SiC/1.4404 (1 vol.%). In contrast to the original feedstock, no annealing colors and only a few powder agglomerations are visible. The components made of alloy SiC/1.4404 (4 vol.%) are characterized by an inhomogeneous surface quality and significant cracks and potential pores are visible as indicated by the red arrows (cf. Figure 8). These extend over the entire height of the component. Annealing colors, however, are not visible. FLG/1.4404 in turn shows a homogeneous surface. Compared to 1.4404, fewer weld spatters are visible, especially on the cylinder. The downskin cone is characterized by annealing colors in the upper half, due to a system failure at layer 500.

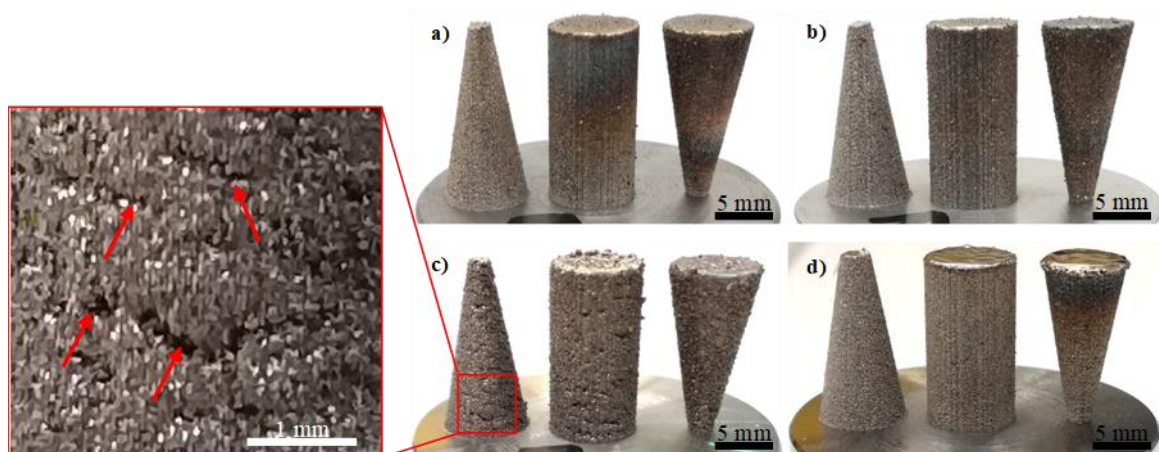


Figure 8: Manufactured components of a) stainless steel 1.4404 powders and its coatings b) SiC/1.4404 (1 vol.%) c) SiC/1.4404 (4 vol.%) and d) FLG/1.4404; red arrows indicate potential cracks and pores at the surface of the specimen

3.6. Relative density

The results of the relative density measurement are shown in Figure 9. Slight defects are noticeable at the upskin cone of the 1.4404 alloy. This involves predominantly the pore formation as illustrated in Table 8. Considering the size of the resulting pores, it is noticeable that most pores are micropores with a size of 10 – 50 μm and located in the upper third of the upskin specimen. Nevertheless, the increased standard deviation is prominent. With increasing component height, the length of the scan vectors decreases. This leads to a consistently changing thermal behavior. This assumption is supported by Figure 7. This results in a non-reproducible and error-prone melting of the material. As illustrated in Table 8, only a decreased amount of inhomogeneities can be detected at the FLG/1.4404 and SiC/1.4404 (1 vol.%) that show almost identical values at all specimens. SiC/1.4404 (4 vol.%), on the contrary, is characterized by an increased amount of defects in the cross-section. In particular, the lack of fusion seems to be a predominant factor as illustrated in Table 8. This is confirmed by the values of relative density. The upskin cone in particular exhibits a relative density of approx. 94 %.

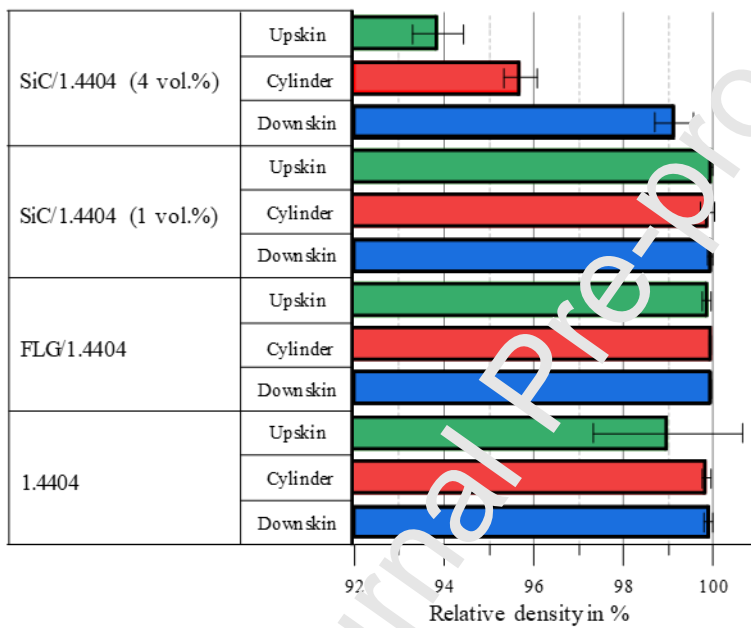
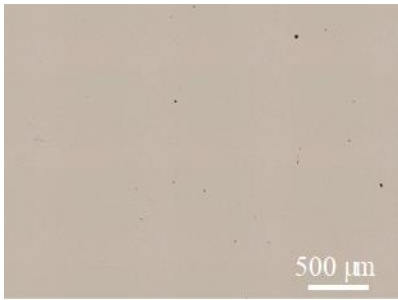
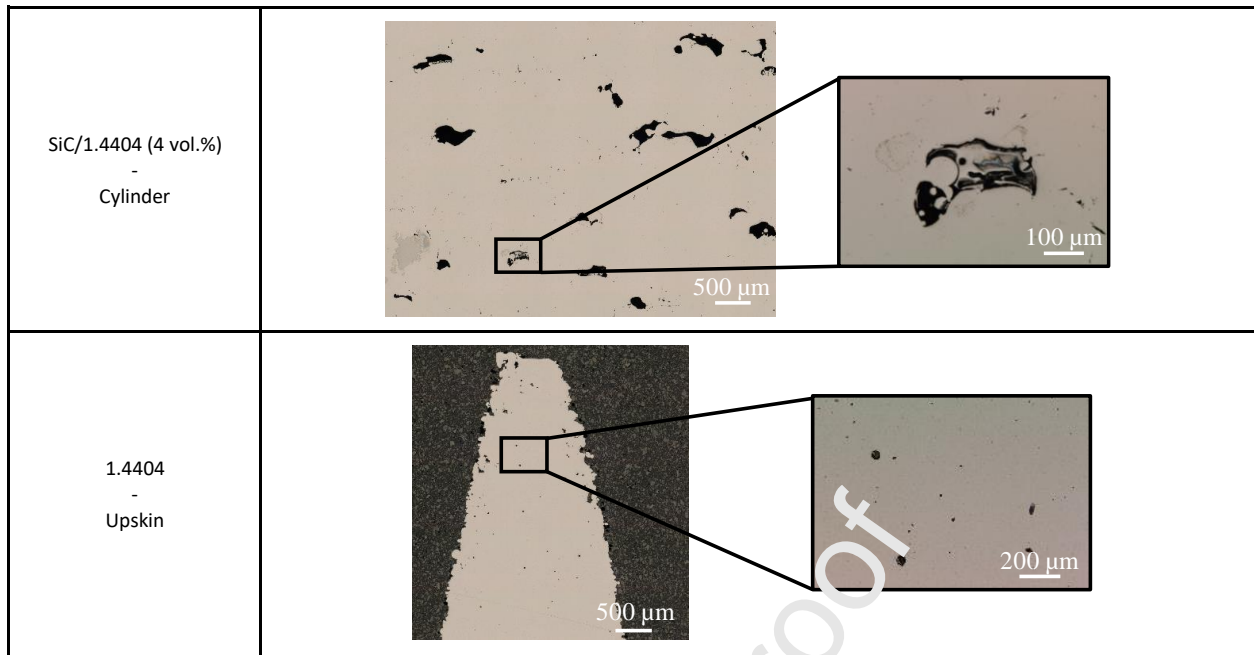


Figure 9: Relative density of manufactured specimens

Table 8: Cross section of manufactured specimens

Specimen	Cross section
SiC/1.4404 (1 vol.%) - Cylinder	



4. Discussion

4.1 Correlation between powder material and temperature

The particle size distribution, morphology and especially the surface roughness of powder particles have a great influence on the degree of reflectance of a material [22,24,25]. Due to multiple scattering of laser radiation, there is a decrease in reflectance with increasing surface roughness. The degree of reflectance of the utilized powder particles is determined by the surface condition resulting from the applied nanoparticle coatings. Thus, the laser radiation is reflected between adjacent powder particles in the powder bed and consequently absorbed in its way as stated by Laumer et al. [45]. Considering Figure 1, it is noticeable that all powder materials exhibit increased sphericity with only a few satellites. This was calculated according to DIN ISO 9276-6:2012-01 [46] and corresponds to a sphericity of 0.974 ± 0.028 . The results show a decreased reflectance simultaneously to an increasing volume content of SiC. Consequently, an increased surface roughness at SiC/1.4404 (4 vol.%) is expected. In first experiments the surface roughness was determined by atomic force microscopy (AFM) (Nanowizard 3, JPK Instruments). In principle, the statement made here was confirmed. However, an analysis of a large number of particles is necessary to be able to make a reliable statement. In addition, only a small area on the particle is considered in the measurement, which includes the surface modification as well as the original surface structure of the feedstock material. Furthermore, especially the alloys SiC/1.4404 (4 vol.%) and FLG/1.4404, the additional layers cause local discoloration of the powder particles. These discolorations can already be perceived when viewed macroscopically, as the latter materials appear much darker as illustrated in Figure 10. The discoloration may have an additional influence on the reflectance considering the wavelength of the laser used, since the color gradation from a lighter to darker gray corresponds to the order of the reflectance measurement.

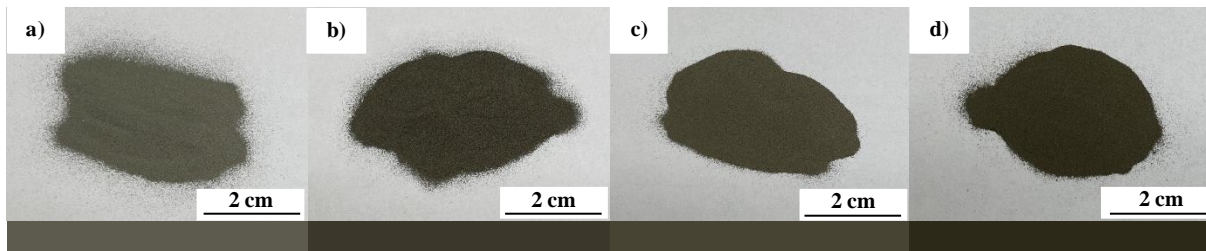


Figure 10: Images of feedstock material a) 1.4404 b) FLG (0.75 vol.%) and SiC surface coated coverages c) 1 vol.% d) 4 vol.% highlighting the discoloration of the powder particles

The SiC coating with an increased volume fraction shows accumulations of particles forming a ring-like shape. This behavior is likely to occur due to drying effects at these relatively high volume fraction. In contrast, the FLG layer deposited on the original feedstock exhibit an island-like shape. Considering the reflectance and temperature values, alloy SiC/1.4404 (4 vol.%), which is characterized by the lowest reflectance values, exhibits the highest temperatures within all layer ranges (cf. Figure 7). Since the same process parameters were used in all build processes, SiC coating has a significant influence on the temperatures occurring in the component, especially with an increased volume fraction. FLG/1.4404, which also shows decreased reflectance behavior, exhibits decreased temperatures in the component and in the surrounding powder bed due to its high thermal conductivity (cf. Table 7). The thermal conductivity of graphene is not constant but increases with the length of a graphene layer at room temperature [47]. The FLG-coated material promotes the formation of a narrow heat-affected zone, as the heat can be rapidly dissipated through the solidified powder material into the build plate. The rapid heat dissipation allows good processability by PBF-LB/M, which is also confirmed by the relative density (cf. Figure 9). A possible concern that rapid heat dissipation could lead to the formation of internal stress and resulting cracks could not be observed.

4.2 Correlation between component geometry and temperature

For each component geometry, a systematic temperature change over the component height is noticeable. While the temperatures within the cylinders remain rather constant, the upskin geometries are characterized by a significant temperature decrease and the downskin geometries by a significant temperature increase. Since the downskin geometry was manufactured without any support structures, the heat generated in the process can be dissipated less effectively into the build plate. The inferior thermal conductivity into the surrounding powder instead of into the underlying solidified layers promotes the formation of increasing temperatures. Körperich et. al. [29] investigated, for example, the temperature change over the height of the component for the hot-working steel 1.2344. They noticed a decrease in temperature in the manufactured cuboid with a constant cross-section. This is in contrast to the constant temperatures within the cylinders manufactured in this work, which also shows no change in cross-section. The dimensions of the cuboid by Körperich et al. result in a surface to volume ratio of 0.422, while the cylinders exhibit a ratio of 0.625. A decreased surface area at a simultaneously large volume of the cuboids is ensured. Since the heat conduction via the surface of the cuboid into the loose powder is lower than the heat conduction via the volume of the already solidified powder material into the build plate, an increased amount of heat can thus be dissipated. The cylinders of this work, on the other hand, have a comparatively large surface but a smaller volume. This results in the opposite case and less heat can be dissipated through the solidified powder material into the build plate. In addition, the material 1.2344 has a thermal conductivity of $\lambda = 25 \text{ W/m}^{\circ}\text{K}$ (at 20°C) which is approx. 67 % higher than the thermal conductivity of 1.4404 ($\lambda = 15 \text{ W/m}^{\circ}\text{K}$ at 20°C). The build process in this work consisted of a total of 533 layers. Accordingly, half of the component height is located at layer 267, where the cross-sectional areas of the upskin and downskin geometries are exactly the same. For both geometries in the layer range 200 – 230, immediately before reaching the center of the component, an intersection of the measured temperature can be observed for all material combinations. This confirms that homogeneous temperatures are obtained for similar-sized cross-sectional areas.

4.3 Correlation between relative density and temperature

The decreased relative density of SiC/1.4404 (4 vol.%) is noticeable. A possible explanation for the formation of large pores could be the formation of so-called incomplete fusion or lack of fusion. The incomplete fusion defects are insufficient fusions of adjacent melt pools, which occur after cooling in form of areas that have not been melted. This type of defect is represented by a cavity containing unmelted or only partially melted powder particles as illustrated at the SiC/1.4404 (4 vol.%) in Table 8. [48,49] This phenomenon occurs mainly horizontally within a layer or vertically over several layers. Although SiC/1.4404 (4 vol.%) is characterized by the highest measured temperatures (cf. Figure 7), the reason might be the irregular process performance. Due to the increased amount of weld spatters that are deposited on the powder bed, a pronounced welding fume can be assumed (cf. Table 6). During the PBF-LB/M-process, this leads to a beam attenuation, beam deflection or focus shift. All powder materials were processed with the same process parameters to ensure comparability. Due to the significantly different melting behavior, an adaption of an individual exposure strategy and process parameters could promote an optimized processing.

5. Conclusion

In this work, the commercially available powder material 1.4404 was coated with the nanoparticles SiC and FLG. After analyzing the reflectance behavior of the powder materials, a standardized build process was performed. The build process was recorded by a systematically calibrated infrared camera to the individual material in order to reveal an in-situ temperature distribution in the powder bed in dependence on the component height. The optical evaluation of the component quality completes the work. Consequently, the following main findings can be derived:

1. The reflectance of modified powder materials could be increased. The main influencing variables are surface roughness and the discoloration of individual powder particles.
2. The degree of reflectance of an alloy is not the only decisive factor for the prevailing temperatures in the powder bed and in the melting zone. The thermal conductivity of the respective materials is attested to have a significant influence on process parameter selection.
3. An increased relative density was achieved by FLG/1.4404 and SiC/1.4404 (1 vol.%). The alloys exhibit less defects than the original feedstock 1.4404 and annealing colors could not be detected.
4. The material SiC/1.4404 (4 vol.%) was difficult to process on the equipment currently in use. The high proportion of hard ceramic particles led to an increased amount of weld spatters during the process and significant bonding defects with the set exposure parameters.

6. Outlook

At first, the surface roughness of coated particles will be analyzed by AFM to validate the effect on the reflectance behavior. Furthermore, according to the Schaeffler diagram [50], the increased carbon content results in an increased Ni-equivalent and thus, in an area that could no longer be weldable due to a possible hot cracking tendency. In this context, the SiC/1.4404 (4 vol.%) material combination is of particular interest. Consequently, in connection with an individual parameter characterization for the modified stainless steel 1.4404 powder materials, a comprehensive microstructural analysis including the investigation of the element distribution (EDX) will be conducted in future studies. In addition, the investigations carried out will be extended with regard to component quality by hardness testing and tensile tests. Statements about further advantages and disadvantages of the coatings concerning the corrosion consequences and thus further possible areas of application will be obtained.

CRedit authorship contribution statement

Oliver Pannitz: Project administration, Conceptualization, Data curation, Investigation, Formal analysis, Methodology, Visualization, Writing – original draft, Writing – review and editing. **Arne**

Lüddecke: Writing – review and editing, Methodology, Resources. **Arno Kwade:** Funding acquisition, Supervision, Resources. **Jan T. Sehr:** Funding acquisition, Supervision, Resources, Writing – review and editing.

Acknowledgments

This work was supported by the Deutsche Forschungsgemeinschaft (DFG, German Research Foundation), priority program „Materials for Additive Manufacturing”, SPP 2122, Grant-ID SE 2935/1-1, Project-ID 410107213. The authors gratefully acknowledge the financial supports.

Declaration of interests

The authors declare that they have no known competing financial interests or personal relationships that could have appeared to influence the work reported in this paper.

The authors declare the following financial interests/personal relationships which may be considered as potential competing interests:

References

- [1] A. Gebhardt, Additive Fertigungsverfahren: Additive Manufacturing und 3D-Drucken für Prototyping - Tooling - Produktion, fifth., neu bearbeitete und erweiterte Auflage, Hanser, München, 2016.
- [2] Deutsches Institut für Normung e. V., Additive Manufacturing - General principles - Terminology, Beuth Verlag GmbH, Berlin 2016.02.25, 2018 (accessed 10 June 2019).
- [3] T.T. Wohlers, Wohlers Report: 3d printing and additive manufacturing state of the industry, WOHLERS Associates, Fort Collins, 2018.
- [4] D. Herzog, V. Seyda, E. Wycisk, C. Emmelmann, Additive manufacturing of metals, *Acta Materialia* 117 (2016) 371–392. <https://doi.org/10.1016/j.actamat.2016.07.019>.
- [5] C.Y. Yap, C.K. Chua, Z.L. Dong, Z.H. Liu, D.Q. Zhang, L.E. Loh, S.L. Sing, Review of selective laser melting: Materials and applications, *Applied Physics Reviews* 2 (2015) 41101. <https://doi.org/10.1063/1.4935926>.
- [6] D. Gu, Y.-C. Hagedorn, W. Meiners, K. Wissenbach, R. Poprawe, Nanocrystalline TiC reinforced Ti matrix bulk-form nanocomposites by Selective Laser Melting (SLM): Densification, growth mechanism and wear behavior, *Composites Science and Technology* 71 (2011) 1612–1620. <https://doi.org/10.1016/j.compscitech.2011.07.010>.
- [7] D. Gu, G. Meng, C. Li, W. Meiners, R. Poprawe, Selective laser melting of TiC/Ti bulk nanocomposites: Influence of nanoscale reinforcement, *Scripta Materialia* 67 (2012) 185–188. <https://doi.org/10.1016/j.scriptamat.2012.04.013>.
- [8] D. Gu, H. Wang, G. Zhang, Selective Laser Melting Additive Manufacturing of Ti-Based Nanocomposites: The Role of Nanopowder, *Metall and Mat Trans A* 45 (2014) 464–476. <https://doi.org/10.1007/s11661-013-1968-4>.
- [9] D. Gu, H. Wang, D. Dai, P. Yuan, W. Meiners, R. Poprawe, Rapid fabrication of Al-based bulk-form nanocomposites with novel reinforcement and enhanced performance by selective laser melting, *Scripta Materialia* 96 (2015) 25–28. <https://doi.org/10.1016/j.scriptamat.2014.10.011>.
- [10] D. Gu, H. Wang, F. Chang, D. Dai, P. Yuan, Y.-C. Hagedorn, W. Meiners, Selective Laser Melting Additive Manufacturing of TiC/AlSi10Mg Bulk-form Nanocomposites with Tailored Microstructures and Properties, *Physics Procedia* 56 (2014) 108–116. <https://doi.org/10.1016/j.phpro.2014.08.153>.
- [11] B. AlMangour, D. Grzesiak, Jenn-Ming Yang, Selective laser melting of TiC reinforced 316L stainless steel matrix nanocomposites: Influence of starting TiC particle size and volume content, *Materials & Design* 104 (2016) 141–151. <https://doi.org/10.1016/j.matdes.2016.05.018>.

- [12] B. AlMangour, D. Grzesiak, J. Cheng, Y. Ertas, Thermal behavior of the molten pool, microstructural evolution, and tribological performance during selective laser melting of TiC/316L stainless steel nanocomposites: Experimental and simulation methods, *Journal of Materials Processing Technology* 257 (2018) 288–301. <https://doi.org/10.1016/j.jmatprotec.2018.01.028>.
- [13] B. AlMangour, D. Grzesiak, J.-M. Yang, Rapid fabrication of bulk-form TiB₂/316L stainless steel nanocomposites with novel reinforcement architecture and improved performance by selective laser melting, *Journal of Alloys and Compounds* 680 (2016) 480–493. <https://doi.org/10.1016/j.jallcom.2016.04.156>.
- [14] Z. Zhao, J. Li, P. Bai, H. Qu, M. Liang, H. Liao, L. Wu, P. Huo, H. Liu, J. Zhang, Microstructure and Mechanical Properties of TiC-Reinforced 316L Stainless Steel Composites Fabricated Using Selective Laser Melting, *Metals* 9 (2019) 267. <https://doi.org/10.3390/met9020267>.
- [15] M.B. Wilms, R. Streubel, F. Frömel, A. Weisheit, J. Tenkamp, F. Walther, S. Barcikowski, J.H. Schleifenbaum, B. Gökce, Laser additive manufacturing of oxide dispersion strengthened steels using laser-generated nanoparticle-metal composite powders, *Proceedia CIRP* 74 (2018) 196–200. <https://doi.org/10.1016/j.procir.2018.08.093>.
- [16] O. Salman, A. Funk, A. Waske, J. Eckert, S. Scudino, Additive Manufacturing of a 316L Steel Matrix Composite Reinforced with CeO₂ Particles: Process Optimization by Adjusting the Laser Scanning Speed, *Technologies* 6 (2018) 25. <https://doi.org/10.3390/technologies6010025>.
- [17] F. Chang, D. Gu, D. Dai, P. Yuan, Selective laser melting of in-situ Al₄SiC₄ + SiC hybrid reinforced Al matrix composites: Influence of starting SiC particle size, *Surface and Coatings Technology* 272 (2015) 15–24. <https://doi.org/10.1016/j.surfcoat.2015.04.029>.
- [18] J.T. Sehr, S. Kleszczynski, C. Notthoff, Nanoparticle improved metal materials for additive manufacturing, *Prog Addit Manuf* 2 (2017) 179–191. <https://doi.org/10.1007/s40964-017-0028-9>.
- [19] J.T. Sehr, S. Kleszczynski, C. Notthoff, M. Lau, B. Gökce, S. Barcikowski, Laser powder bed fusion of nano-WC-modified and nano-TiO₂-modified metal powders, *Proceedings of International Conference on Additive Technologies* 6 (2016) 26–38.
- [20] B. Zhang, L. Dembinski, C. Codder, The study of the laser parameters and environment variables effect on mechanical properties of high compact parts elaborated by selective laser melting 316L powder, *Materials Science and Engineering: A* 584 (2013) 21–31. <https://doi.org/10.1016/j.msea.2013.06.055>.
- [21] J.T. Sehr, Möglichkeiten und Grenzen bei der generativen Herstellung metallischer Bauteile durch das Strahlschmelzverfahren. Zugl.: Duisburg-Essen, Univ., Diss., 2010, Shaker, Aachen, 2010.
- [22] W. Zhou, X. Sun, K. Kobayashi, N. Nomura, K. Yoshimi, A. Kawasaki, Carbon nanotubes as a unique agent to fabricate nanoceramic/metal composite powders for additive manufacturing, *Materials & Design* 157 (2018) 276–285. <https://doi.org/10.1016/j.matdes.2017.10.034>.
- [23] Y. Yang, D. Gu, D. Dai, C. Ma, Laser energy absorption behavior of powder particles using ray tracing method during selective laser melting additive manufacturing of aluminum alloy, *Materials & Design* 143 (2018) 12–19. <https://doi.org/10.1016/j.matdes.2018.01.043>.
- [24] D. Gu, Y. Yang, L. Xi, J. Yang, M. Xia, Laser absorption behavior of randomly packed powder-bed during selective laser melting of SiC and TiB₂ reinforced Al matrix composites, *Optics & Laser Technology* 119 (2019) 105600. <https://doi.org/10.1016/j.optlastec.2019.105600>.
- [25] C.D. Boley, S.A. Khairallah, A.M. Rubenchik, Calculation of laser absorption by metal powders in additive manufacturing (2014).
- [26] N.K. Tolochko, Y.V. Khlopkov, S.E. Mozzharov, M.B. Ignatiev, T. Laoui, V.I. Titov, Absorptance of powder materials suitable for laser sintering, *Rapid Prototyping Journal* 6 (2000) 155–161. <https://doi.org/10.1108/13552540010337029>.
- [27] J.L. Bartlett, F.M. Heim, Y.V. Murty, X. Li, In situ defect detection in selective laser melting via full-field infrared thermography, *Additive Manufacturing* 24 (2018) 595–605. <https://doi.org/10.1016/j.addma.2018.10.045>.

- [28] H. Krauss, C. Eschey, M.F. Zaeh, Thermography for Monitoring the Selective Laser Melting Process, Proceedings of the solid freeform fabrication symposium (2012).
- [29] J.P. Körperich, M. Merkel, Thermographic analysis of the building height impact on the properties of tool steel in selective laser beam melting, *Materialwiss. Werkstofftech.* 49 (2018) 689–695. <https://doi.org/10.1002/mawe.201800010>.
- [30] L. Zheng, Q. Zhang, H. Cao, W. Wu, H. Ma, X. Ding, J. Yang, X. Duan, S. Fan, Melt pool boundary extraction and its width prediction from infrared images in selective laser melting, *Materials & Design* 183 (2019) 108110. <https://doi.org/10.1016/j.matdes.2019.108110>.
- [31] J.O. Milewski, Additive Manufacturing of Metals: From Fundamental Technology to Rocket Nozzles, Medical Implants, and Custom Jewelry, Springer International Publishing, Cham, 2017.
- [32] M.R. Alkahari, T. Furumoto, T. Ueda, A. Hosokawa, R. Tanaka, M.S. Abdul Aziz, Thermal Conductivity of Metal Powder and Consolidated Material Fabricated via Selective Laser Melting, *KEM* 523-524 (2012) 244–249. <https://doi.org/10.4028/www.scientific.net/KEM.523-524.244>.
- [33] D. Buchbinder, H. Schleifenbaum, S. Heidrich, W. Meiners, J. Füllmann, High Power Selective Laser Melting (HP SLM) of Aluminum Parts, *Physics Procedia* 12 (2011) 271–278. <https://doi.org/10.1016/j.phpro.2011.03.035>.
- [34] J.C. Simmons, X. Chen, A. Azizi, M.A. Daeumer, P.Y. Zavaliy, C. Zhou, S.N. Schiffres, Influence of processing and microstructure on the local and bulk thermal conductivity of selective laser melted 316L stainless steel, *Additive Manufacturing* 32 (2020) 100996. <https://doi.org/10.1016/j.addma.2019.100996>.
- [35] Deutsches Institut für Normung e. V., Nichtrostende Stähle - Teil 1: Verzeichnis der nichtrostenden Stähle, Beuth Verlag GmbH, Berlin 17.140.20, 2014 (accessed 15 June 2019).
- [36] Deutsches Institut für Normung e. V., Partikelgrößenanalyse – Dynamische Lichtstreuung (DLS), Beuth Verlag GmbH, Berlin 19.120, 2018 (accessed 20 November 2020).
- [37] K. Meyer, Nanomaterialien als Fließregulierungsmittel. Dissertation, Würzburg, 2003.
- [38] H. Krauss, Qualitätssicherung beim Laserschmelzen durch schichtweise thermografische In-Process-Überwachung.
- [39] G. Lagaly, O. Schulz, R. Zimehl, Dispersionen und Emulsionen: Eine Einführung in die Kolloidik feinverteilter Stoffe einschließlich der Tonminerale, Steinkopff, Heidelberg, 1997.
- [40] T. Breinlinger, T. Kraft, A simple method for simulating the coffee stain effect, *Powder Technology* 256 (2014) 279–284. <https://doi.org/10.1016/j.powtec.2014.02.024>.
- [41] R.D. Deegan, O. Bakajin, F.F. Dupont, G. Huber, S.R. Nagel, T.A. Witten, Capillary flow as the cause of ring stains from dried liquid drops, *Nature* 389 (1997).
- [42] P.J. Yunker, T. Still, M.A. Lohr, A.G. Yodanis, Suppression of the coffee-ring effect by shape-dependent capillary interactions, *Nature* 476 (2011) 308–311. <https://doi.org/10.1038/nature10344>.
- [43] H. Hu, R.G. Larson, Evaporation of a Sessile Droplet on a Substrate, *J. Phys. Chem. B* 106 (2002) 1334–1344. <https://doi.org/10.1021/jp0118322>.
- [44] N.D. Denkov, O.D. Velev, P.A. Kralchevsky, I.B. Ivanov, H. Yoshimura, K. Nagayama, Two-dimensional crystallization, *Nature* 361 (1993).
- [45] T. Laumer, K. Wudy, M. Drexler, P. Amend, S. Roth, D. Drummer, M. Schmidt, Fundamental investigation of laser beam melting of polymers for additive manufacture, *Journal of Laser Applications* 26 (2014) 42003. <https://doi.org/10.2351/1.4892848>.
- [46] Deutsches Institut für Normung e. V., Darstellung der Ergebnisse von Partikelgrößenanalysen, Beuth Verlag GmbH, Berlin 19.120 (accessed 18 November 2020).
- [47] X. Xu, L.F.C. Pereira, Y. Wang, J. Wu, K. Zhang, X. Zhao, S. Bae, C. Tinh Bui, R. Xie, J.T.L. Thong, B.H. Hong, K.P. Loh, D. Donadio, B. Li, B. Özyilmaz, Length-dependent thermal conductivity in suspended single-layer graphene, *Nat. Commun.* 5 (2014) 3689. <https://doi.org/10.1038/ncomms4689>.
- [48] Q.C. Liu, J. Elambasseril, S.J. Sun, M. Leary, M. Brandt, P.K. Sharp, The Effect of Manufacturing Defects on the Fatigue Behaviour of Ti-6Al-4V Specimens Fabricated Using

Selective Laser Melting, AMR 891-892 (2014) 1519–1524.

<https://doi.org/10.4028/www.scientific.net/AMR.891-892.1519>.

[49] T. Mukherjee, J.S. Zuback, A. De, T. DebRoy, Printability of alloys for additive manufacturing, Sci. Rep. 6 (2016) 19717. <https://doi.org/10.1038/srep19717>.

[50] E. Roos, K. Maile, M. Seidenfuß, Werkstoffkunde für Ingenieure, Springer Berlin Heidelberg, Berlin, Heidelberg, 2017.

Graphical abstract

Highlights

- Stainless steel powder 1.4404 is successfully coated with silicon carbide and few-layer graphene.
- The developed silicon carbide and few-layer graphene coated 1.4404 powder exhibits a decreased reflectance.
- Silicon carbide (1 vol.%) and few-layer graphene (0.75 vol %) coatings improve the relative density of upskin specimens to 99.9 %.
- The addition of silicon carbide (4 vol.%) leads to a decrease in relative density of approx. 93.9 %.
- The few-layer graphene coating leads to a rapid heat dissipation into the already solidified underlying layers during the melting process.